PDMS-Assisted Low-Temperature Synthesis of Submillimeter All-Inorganic Halide Perovskite Microcrystals for High-Performance Photodetectors

*Zhengxun Lai, You Meng, Fei Wang, Xiuming Bu, Dong Chen, Pengshan Xie, Weijun Wang, Dengji Li, Yuxuan Zhang, Wei Wang, Chuntai Liu, SenPo Yip, and Johnny C. Ho**

All-inorganic halide perovskites (AIHPs) are promising photovoltaic materials that have been extensively studied in the last decade. In addition, lead-free AIHPs are preferred because of their non-toxic and environmentally friendly nature. However, the quality of AIHPs fabricated by conventional solution processing methods is usually unsatisfactory, which leads to poor photo-electric performance. Herein, a facile polydimethylsiloxane-assisted slow evaporation method that can be readily used to synthesize high-quality AIHP microcrystals (MCs) ($CsPbBr_3$, $Cs_2AgBiBr_6$, and L-$Cs_3Sb_2I_9$) is demonstrated. The photodetection properties of the synthesized AIHP MCs and their spin-coated thin-film counterparts are thoroughly studied and compared. Owing to their superior crystallinity, AIHP MCs show better photoelectric perfor-mance than spin-coated films. The responsivity of the $CsPbBr_3$ microcrystal photodetectors is ≈590 000 mA W^{-1}. This work proposes a universal solution-processing method for the successful fabrication of high-quality all-inorganic lead-based ($CsPbBr_3$), lead-free (L-$Cs_3Sb_2I_9$), and double ($Cs_2AgBiBr_6$) perovskites, which can overcome the bottleneck in the development of halide perovskites and promote their applications.

1. Introduction

Halide perovskites are very promising materials for active devices used in high-efficiency photodetectors, solar cells, and light-emitting diodes.[1–3] Owing to their excellent photoelec-tric properties, these perovskites have been recently used in extensive studies.[4–6] However, the organic cations in organic–

inorganic halide perovskites are very sen-sitive to high temperatures and moisture, leading to poor device stability in ambient environments. Fortunately, all-inorganic halide perovskites (AIHPs) exhibit better stability as they are configured without any organic cations. It is well accepted that Cs^+ is the most suitable inorganic cation to replace organic cations owing to its sufficiently large size facilitating its incorporation into these ABX_3 perovskite structures with an appropriate tolerance factor.[7] Although the narrow bandgap of $CsPbI_3$ (more generally $CsPbX_3$ [X = I, Br, or Cl]) makes it more suitable for solar cells, its poor structural stability hinders further applications. For $CsPbCl_3$, the poor solubility of CsCl and $PbCl_2$ make it difficult to be synthesized by solution-based methods.[8,9] Similarly, $CsPbBr_3$ has a bandgap of 2.36 eV, making it a good material choice as an active channel for visible light detection, which is beneficial for commercialization. Nevertheless, there are still many chal-lenges associated with $CsPbBr_3$-based photodetectors. First, the complicated Cs-Pb-Br phase diagrams make it difficult to obtain pure $CsPbBr_3$ with optimal photoelectric properties during synthesis.[10] In addition, the performance of $CsPbBr_3$-based photodetectors is not satisfactory due to the relatively low solubility of CsBr, especially in devices fabricated by

Z. X. Lai, Y. Meng, F. Wang, X. M. Bu, D. Chen, P. S. Xie, W. J. Wang, D. J. Li, Y. X. Zhang, W. Wang, J. C. Ho
Department of Materials Science and Engineering
City University of Hong Kong
Hong Kong 999077, China
E-mail: johnnyho@cityu.edu.hk

F. Wang
State Key Laboratory of Luminescence and Applications
Changchun Institute of Optics
Fine Mechanics and Physics
Chinese Academy of Sciences
Changchun 130021, China

F. Wang, W. Wang, J. C. Ho
State Key Laboratory of Terahertz and Millimeter Waves
City University of Hong Kong
Hong Kong 999077, China

C. Liu
Key Laboratory of Advanced Materials Processing & Mold
(Zhengzhou University)
Ministry of Education
Zhengzhou 450002, China

S. P. Yip, J. C. Ho
Institute for Materials Chemistry and Engineering
Kyushu University
Fukuoka 816–8580, Japan

**ADVANCED
SCIENCE NEWS**

www.advancedsciencenews.com

**ADVANCED
OPTICAL
MATERIALS**

www.advopticalmat.de

solution-processing methods. Moreover, high annealing temperatures (≈200–350 °C) required for obtaining high-quality spin-coated AIHPs pure-phase films are a major hindering factor for their subsequent studies and applications. Furthermore, a high annealing temperature would inevitably destroy other functional layers during the fabrication of photovoltaic devices.[11] In this regard, a simple low-temperature solution-processing method to fabricate high-quality $CsPbBr_3$ with high photodetection performances is thus urgently needed.

Lead-free AIHPs are even preferred over lead-based ones, owing to their nontoxic nature. $Cs_2AgBiBr_6$ is a promising AIHP material with good stability, which has been utilized in different optoelectronic devices. In $Cs_2AgBiBr_6$, the monovalent metal Ag^+ and trivalent metal Bi^{3+} are used to replace two Pb^{2+} (see Figures S1a, Supporting Information, for (cubic $CsPbBr_3$) and S1b, Supporting Information, for ($Cs_2AgBiBr_6$)), hence the double perovskite name is given to it. Even though lead-free $Cs_2AgBiBr_6$ is a promising double perovskite widely applied in photovoltaic devices, its photoelectric performance is still far from catching up with lead-based ones. Furthermore, Bi^{3+} or Sb^{3+} can be used to substitute Pb^{2+} in $CsPbX_3$, forming a $Cs_3B_2X_9$ (B = Bi^{3+} or Sb^{3+}) structure. This type of lead-free AIHPs (i.e., $Cs_3Sb_2I_9$) has been previously studied and explored for photovoltaic applications.[12–15] Although solution-processing methods, including spin coating, are facile and preferred for industrial production, the poor crystallinity of the obtained solution-processed $Cs_3Sb_2I_9$ leads to unsatisfactory optoelectronic performances.[16,17] More importantly, two phases of $Cs_3Sb_2I_9$ are available, with distinct properties: the dimer phase, $D-Cs_3Sb_2I_9$ (Figure S1c, Supporting Information) and the layered phase, $L-Cs_3Sb_2I_9$ (Figure S1d, Supporting Information).[18,19] The $D-Cs_3Sb_2I_9$ phase has an indirect bandgap and poor photoelectric properties; therefore, its formation is typically avoided during synthesis process. Although the layered $L-Cs_3Sb_2I_9$ phase is preferred owing to its enhanced properties, $L-Cs_3Sb_2I_9$ can hardly be synthesized using the solution-processing method.[18,19] Therefore, an effective solution-based method to fabricate high-quality $Cs_2AgBiBr_6$ and $L-Cs_3Sb_2I_9$ is necessary for further development and applications.

In this study, we successfully developed and demonstrated a facile low-temperature solution-processing technique, known as the polydimethylsiloxane (PDMS)-assisted slow evaporation (PASE) method, by which submillimeter-scale high-quality $CsPbBr_3$ MCs were reliably fabricated. In addition, lead-free $Cs_2AgBiBr_6$ and $L-Cs_3Sb_2I_9$ MCs can be fabricated using this universal method. The crystallinity and optical properties of the MCs were carefully characterized, and their photodetection properties were evaluated in photodetectors configurations. Interestingly, the responsivity of $CsPbBr_3$ MC-based photodetectors is as large as 5.9×10^5 mA W^{-1}, which is much larger compared to those based on state-of-the-art solution-processed AIHPs. Moreover, the photodetectors' responsivities with lead-free $Cs_2AgBiBr_6$ and $L-Cs_3Sb_2I_9$ MCs as active layers can reach 3062 and 670 mA W^{-1}, respectively. These results suggest that PASE is a facile and effective solution-processing method for fabricating high-quality AIHPs, which will contribute to the substantial development and applications of halide perovskites.
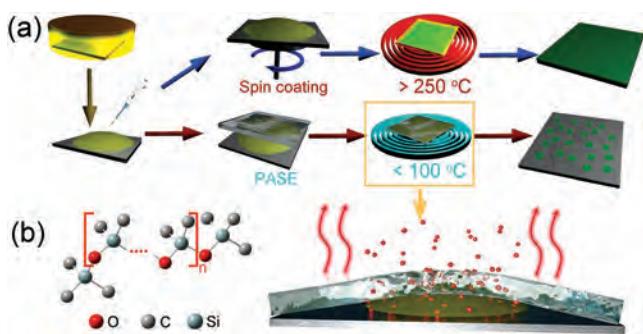
Figure 1. a) Schematic illustration of the PASE method, where the bottom inset shows the schematic of the solvent evaporation process in this method. b) Molecular structure of PDMS.

2. Results and Discussions

As shown in **Figure 1**a, in the conventional spin-coating method, the solvent of the precursor solution volatilizes dramatically in a few seconds, and then, the perovskite material precipitates immediately through numerous nucleation sites across the substrate. Thus, polycrystalline films of unsatisfactory quality are usually obtained. To avoid such spin-coating-induced crystal defects, the PASE method was proposed with the assistance of PDMS. As shown in Figure 1b, the PDMS polymer is composed of Si—O units with abundant —CH_3 substituents, which endows it with excellent hydrophobic and organophilic properties.[20] Hence, PDMS membranes are often used in the areas of pervaporation and separation of organic compounds.[21,22] In this work, PDMS membranes were employed to decrease the evaporation of the solvent. Specifically, during PASE processing, the glass or silicon substrates were first ultrasonically cleaned and then treated with oxygen plasma to render the surface hydrophilic. Subsequently, ≈4 µL of $CsPbBr_3$, $Cs_2AgBiBr_6$, or $Cs_3Sb_2I_9$ solutions were dripped onto the substrates, spread for several seconds, and immediately covered with one PDMS piece. The entire sample stack was then transferred to a hot plate to allow the solvent to evaporate slowly. After ≈3 h, the large-scale AIHP MCs were obtained. As illustrated in Figure 1a, after covering the precursor solution with PDMS, the organic solvents, such as dimethylformamide (DMF) and dimethylsulfoxide (DMSO), will seep into PDMS first because of the unique permeability to the organic molecules of PDMS, and the solvent can then volatilize gradually over several hours. Consequently, submillimeter-scale high-quality crystalline halide perovskite MCs can be acquired. In addition, compared to the conventional spin-coating method, this PASE method uses only a small amount of precursor solution, which can save chemicals, improve efficiency, and be conducive to mass production in the future since most of the solution is usually swung off in the conventional spin-coating method. Importantly, the annealing temperature in the PASE method is as low as 100 °C, which is beneficial for further studies and applications.

The obtained $CsPbBr_3$ MCs were characterized by X-ray diffraction (XRD), as shown in **Figure 2**a. Peaks from the (100), (110), and (200) planes were clearly identified, indicating that pure cubic-phase $CsPbBr_3$ MCs were obtained (PDF #75-0412) without other Cs-Pb-Br phases. As depicted in Figure 2b, UV–vis absorption and photoluminescence (PL) measurements
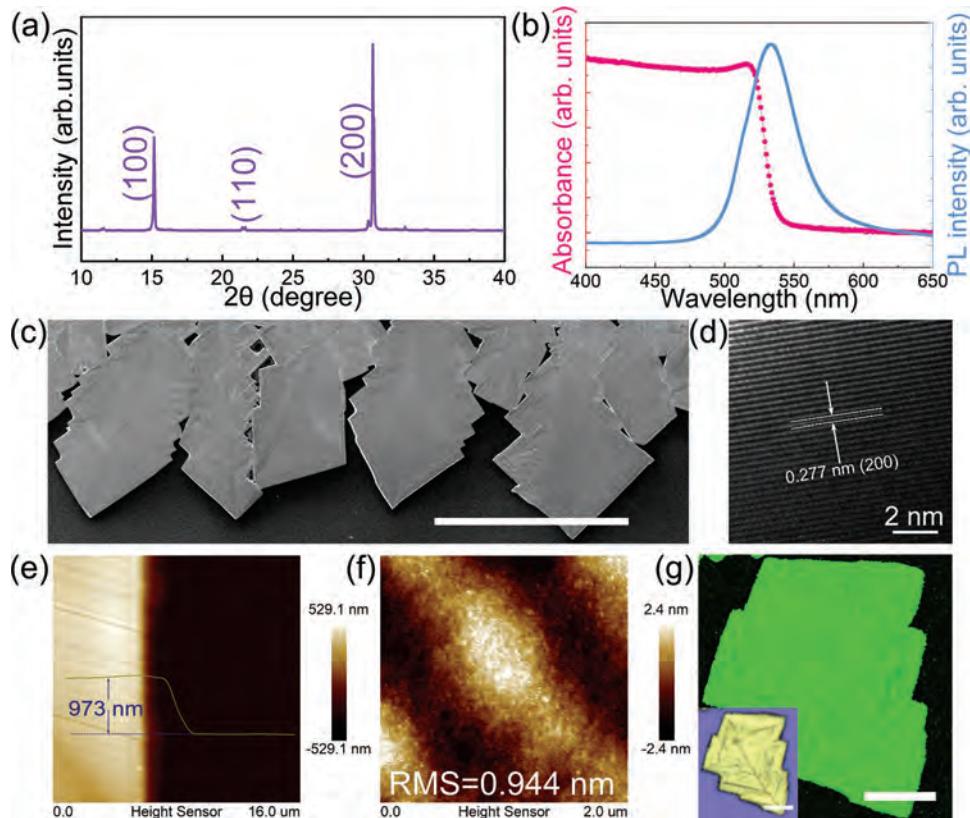
Figure 2. a) XRD pattern, b) absorption and PL spectra, c) SEM image (the scale bar is 500 μm), d) HRTEM image, e) large area AFM image, and f) high-resolution AFM image of the CsPbBr$_3$ MCs. g) PL mapping and the corresponding optical photograph (both scale bars are 70 μm).

were performed to examine the bandgap and luminescence characteristics. The absorption edge of the CsPbBr$_3$ MCs in the absorption spectrum was located at 529 nm, suggesting a bandgap gap of 2.34 eV. The sharp PL peak was located at 534 nm, which confirmed that a direct-bandgap pure-phase cubic CsPbBr$_3$ MCs was obtained. A scanning electron microscopy (SEM) image of the MCs is also shown in Figure 2c, where the scale bar is 500 μm. The lateral dimensions of the leaf-like CsPbBr$_3$ MCs were hundreds of micrometers. A high-resolution transmission electron microscopy (HRTEM) image of the MCs was also obtained to investigate the lattice structure, as shown in Figure 2d. The clear lattice spacing fringes indicate high crystallinity with a lattice distance of 0.277 nm, which corresponds to the (200) plane of the cubic CsPbBr$_3$. Then, a large-area AFM image was obtained to determine the thickness of the MCs (Figure 2e), which was found to be ≈973 nm. A close-up AFM image of the MC surface is depicted in Figure 2f, revealing an ultra-smooth surface morphology with a root-mean-square roughness (RMS) of only 0.944 nm. In addition, as shown in Figure 2g, PL mapping of a typical CsPbBr$_3$ MC was also performed, and the inset shows the corresponding optical image. The uniform photoluminescence of MC confirms its high crystallinity without any obvious defects. In addition, a CsPbBr$_3$ film was also fabricated by the one-step spin-coating method as a control sample and characterized by XRD. As shown in Figure S2a, Supporting Information, several peaks were observed and

assigned to the (100), (110), (200), and (211) planes of cubic CsPbBr$_3$. The UV–vis absorption spectrum with an obvious exciton peak and sharp PL spectrum of the control film are illustrated in Figure S2b, Supporting Information, showing relatively good crystallinity with a direct bandgap of 2.37 eV. An SEM image of the control CsPbBr$_3$ film is also shown in Figure S3, Supporting Information, where there are clear crystalline grains without pinholes. The thickness of the film (121 nm) was determined using AFM (Figure S4, Supporting Information). It is well known that CsPbBr$_3$ films fabricated by conventional spin coating usually suffer from very poor film quality with many pinholes.[23,24] For these control samples, an antisolvent was used during the spinning step, which has been proven to be an effective technique to improve the quality of spin-coated perovskite films.

The CsPbBr$_3$ MCs were then configured as photodetectors with gold electrodes, and the photodetection performance was investigated. The device and measurement schematic are shown in **Figure 3**a. The current–voltage (I–V) curves of the device under dark conditions and different light intensities are shown in Figure S5, Supporting Information. The linear relationship of the I–V curves indicates a nearly ohmic contact between the MCs and electrodes, which is beneficial in devices' application for efficient photo-generated carrier collection. The photocurrents of the devices under illumination with different light intensities were then measured, as shown in Figure 3b. A sublinear relationship between the photocurrent, I, and light
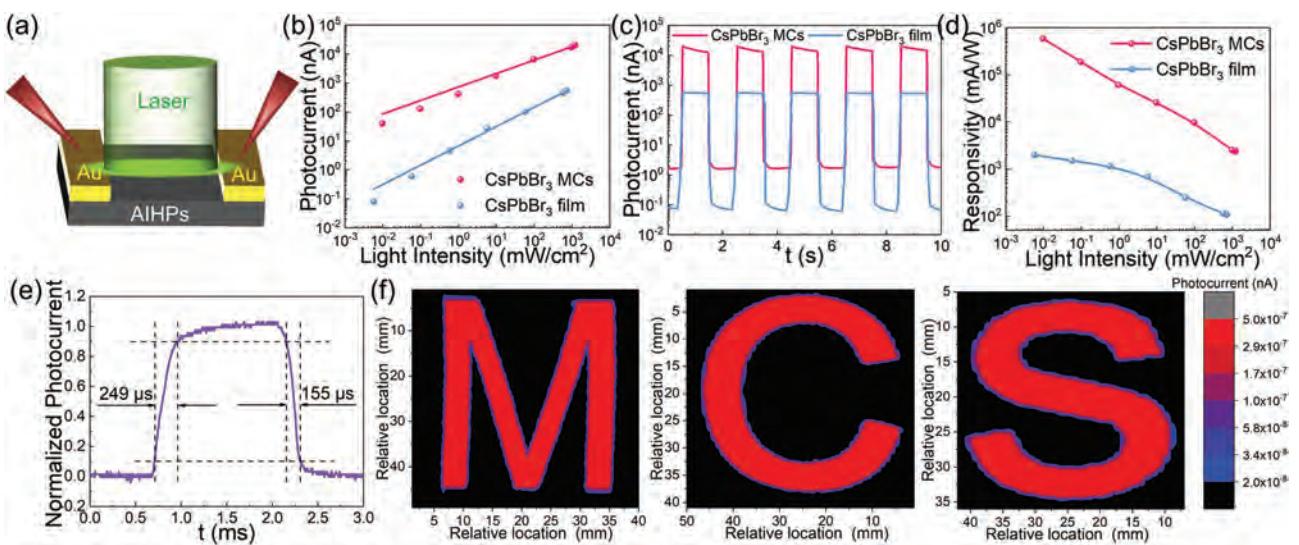
Figure 3. a) Device and measurement schematic. b) Dependence of the photocurrent on the light intensity, c) current versus time curves under a chopped laser, and d) dependence of the responsivity on the light intensity of the CsPbBr$_3$ MCs and film. e) High-resolution current versus time curve for the CsPbBr$_3$ MCs. f) Imaging results of the fabricated CsPbBr$_3$ MCs photodetector.

intensity, P, can be observed, which can be described by $I = AP^\beta$ (A and β are the fitting parameters), as shown in Figure 3b.[25] The β parameter is determined as 0.46 and 0.67 for the CsPbBr$_3$ MCs and spin-coated films, respectively. This sublinear relationship between I and P has resulted from the complex processes of electron-hole generation, trapping, and recombination, which are typically observed in semiconducting materials.[26,27] At the same time, the linear dynamic range (LDR) is a crucial parameter for evaluating the linear light intensity response range for a photodetector, which can be expressed as $\text{LDR} = 20 \log \frac{P_{max}}{P_{min}}$, where P_{max} represents the maximum light intensity limit within linearity, and P_{min} denotes the minimum light intensity.[28,29] According to this formula, the LDR value of the MCs photodetector was determined to be 102 dB. It is worth mentioning that the light intensities, P_{max} and P_{min} used in this study, have reached the intensity limit of the laser; the actual LDR value is supposed to be larger than the calculated value. The time-dependent current response (I–t) curves of the photodetectors configured with active channels of MCs and the control film were also recorded under modulated illumination of a 450 nm laser with an intensity of 900 mW cm^{-2} (Figure 3c). The measured current exhibits clear stable and reproducible on–off switching characteristics. The photocurrent of the MCs photodetector was more than 28 times larger than that of the control film, while the on/off current ratio of the MC-based photodetector was ≈10^4. Moreover, the responsivity (R), which describes the ratio between the photocurrent and incident light power at a given wavelength of light, is also one of the most important parameters for evaluating the performance of photodetectors.[30] Accordingly, it can be calculated using $R = \frac{I}{\Phi S}$, where I, Φ, and S represent the photocurrent, light intensity, and active area of the photodetector, respectively. As shown in Figure 3d, the responsivities of the devices under illumination with different light intensities were compiled. The largest

responsivity of 590 000 mA W^{-1} for the CsPbBr$_3$ MCs photodetector was achieved, which is almost 300 times larger than that of the control film and much larger than that of most state-of-the-art AIHP photodetectors fabricated by solution-processing methods or other techniques such as chemical vapor deposition (CVD) or evaporation.[31–34] Furthermore, the detectivity (D^*) and external quantum efficiency (EQE) are other significant parameters related to R, such as $D^* = RS^{1/2}/(2eI_d)^{1/2}$ and $EQE = hcR/e\lambda$, where e is the electronic charge, I_d is the dark current of the device, h is Planck's constant, c is the velocity of light, and λ is the wavelength of the incident light.[35] It should be noted that D^* is related to the noise source of the photodetector, which corresponds to the dark current, I_d, in this work.[36] The D^* and EQE values for the photodetectors under different light intensities were calculated and are shown in Figure S6, Supporting Information. Similar to the responsivity, the EQE and D^* values of the CsPbBr$_3$ MCs device were still much larger than those of the control film device. The largest EQE and D^* values reach 1.67×10^5% and 7×10^{13} Jones, respectively. In addition, a high response speed is crucial for highly performing photodetectors. In this manner, the response speeds (i.e., the time required for the current to increase from 10% to 90% [rise time] and the time to decrease from 90% to 10% of the peak value [decay time]) of the CsPbBr$_3$ MCs photodetector were investigated, which can be determined from the high-resolution I–t curve as shown in Figure 3e. Efficient rise and decay times of 249 and 155 µs were achieved, respectively. To further demonstrate the excellent response of the CsPbBr$_3$ MCs photodetector, its imaging capability was assessed using a self-assembled imaging system, as depicted in Figure 3f. In the imaging system, the masks of carved letters "M," "C," and "S" are used to acquire the corresponding image. One can see that the clear patterns of the letters are obtained under the illumination of a laser with a wavelength of 532 nm, which is attributable to the high photocurrent and on/off current ratio of the device.

**ADVANCED
SCIENCE NEWS**

www.advancedsciencenews.com

**ADVANCED
OPTICAL
MATERIALS**

www.advopticalmat.de
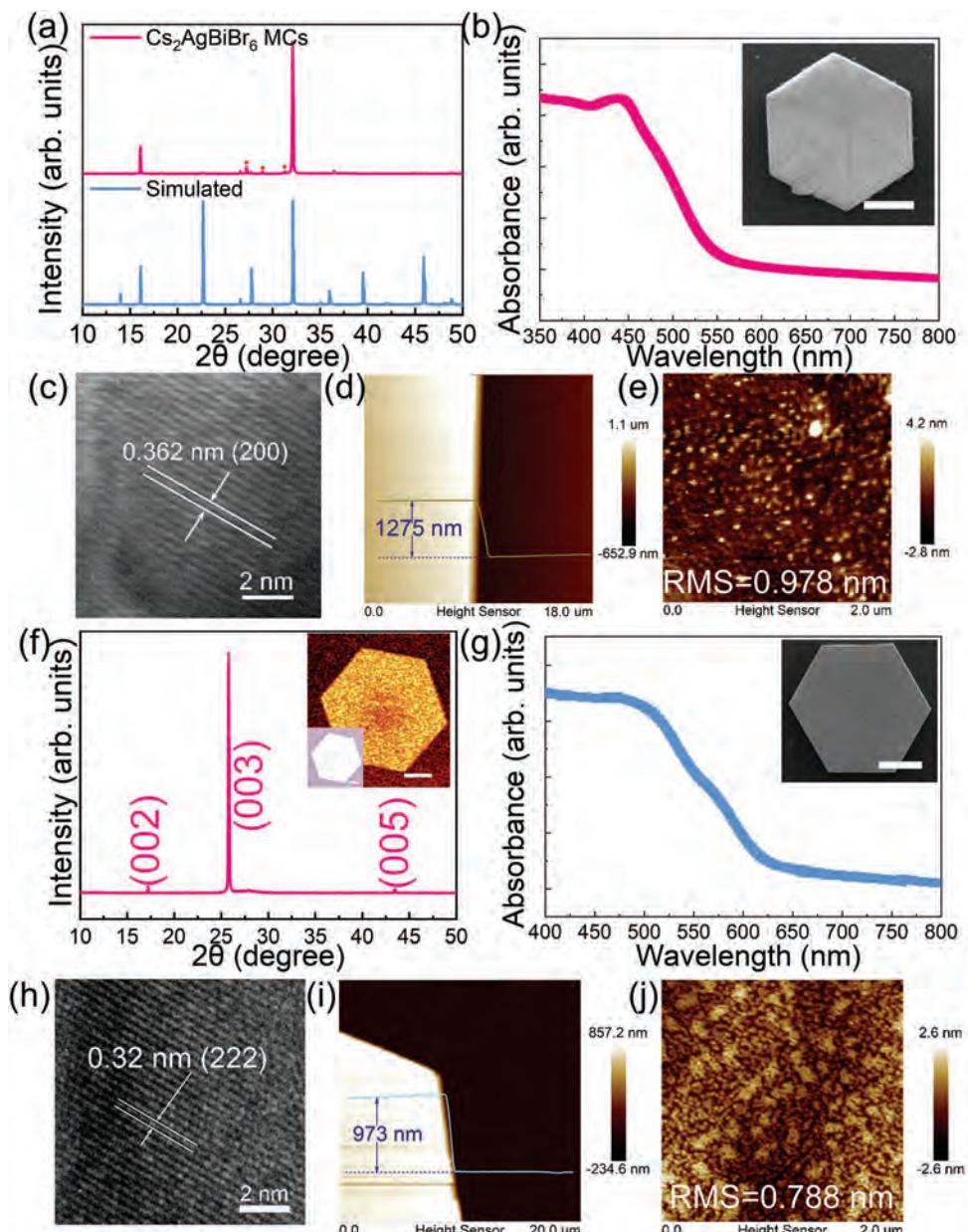
Figure 4. a) Measured and simulated XRD patterns, b) absorption spectrum, where the inset shows the SEM image (the scale bar is 20 µm), c) HRTEM image, d) large area AFM image, e) high-resolution AFM image of the $Cs_2AgBiBr_6$ MCs. f) XRD pattern, where the inset shows the PL mapping and the corresponding optical photograph (both scale bars are 10 µm); g) absorption spectrum, where the inset shows the SEM image (the scale bar is 30 µm); h) HRTEM image; i) large area AFM image; and j) high-resolution AFM image of the $L-Cs_3Sb_2I_9$ MCs.

Similar to $CsPbBr_3$, this universal PASE method can be applied to other AIHPs including $Cs_2AgBiBr_6$ and $L-Cs_3Sb_2I_9$. The XRD pattern of the $Cs_2AgBiBr_6$ MCs fabricated using this method and the simulated pattern are shown in **Figure 4**a. In addition to the intense peaks of $Cs_2AgBiBr_6$, three weak peaks corresponding to $Cs_3Bi_2Br_9$ (marked by red circles) were observed. In fact, residual $Cs_3Bi_2Br_9$ cannot be avoided during the synthesis of $Cs_2AgBiBr_6$.[37,38] As depicted in Figure 4b, the UV–vis absorption spectrum suggests an absorption edge located at 500 nm with a bandgap of 2.48 eV. The SEM image of a typical $Cs_2AgBiBr_6$ MC is shown in the inset of Figure 4b,

and a large-area SEM image is presented in Figure S7, Supporting Information. It can be seen that well-defined MCs were acquired with an edge length of ≈30–40 µm. HRTEM measurements were also performed on $Cs_2AgBiBr_6$ MCs, as shown in Figure 4c. A lattice spacing of 0.362 nm was observed, corresponding to the (200) plane of $Cs_2AgBiBr_6$. The thickness of these MCs can be determined through AFM measurements, which is found at ≈1.3 µm (Figure 4d). A close-up of the AFM image is shown in Figure 4e. The surface topography of the MCs was very smooth, with an RMS of only 0.978 nm. The XRD pattern, UV–vis absorption spectrum, and SEM image

**ADVANCED
SCIENCE NEWS**

www.advancedsciencenews.com

**ADVANCED
OPTICAL
MATERIALS**

www.advopticalmat.de
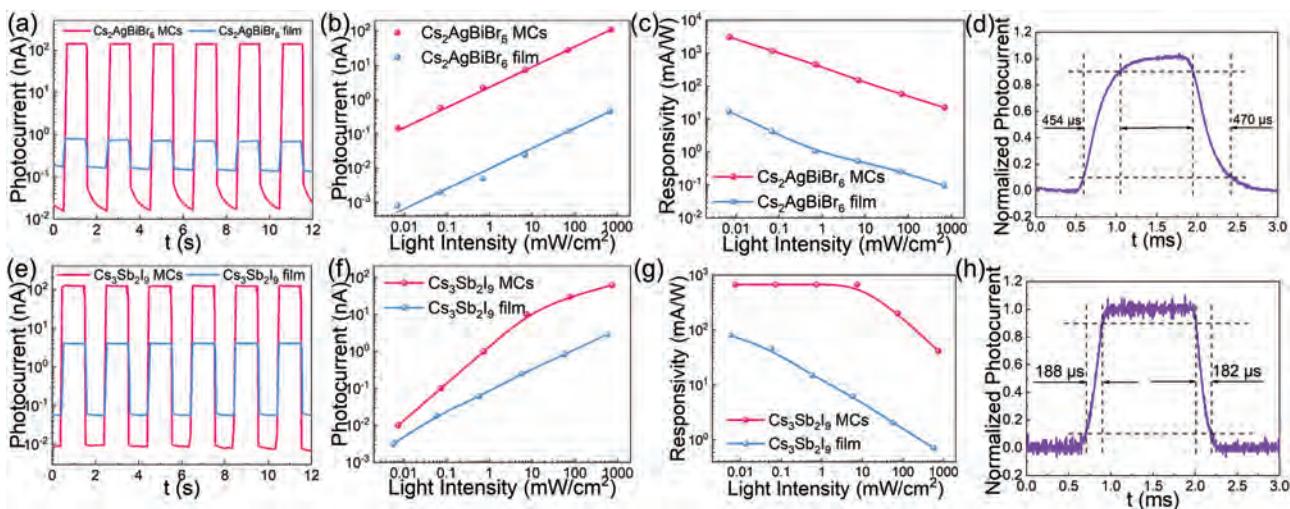
Figure 5. a) Time-dependent photoresponse, b) dependence of the photocurrent on the light intensity, c) dependence of the responsivity on the light intensity of the $Cs_2AgBiBr_6$ MCs and film. d) High-resolution current versus time curve for the $Cs_2AgBiBr_6$ MCs. e) Time-dependent photoresponse, f) dependence of the photocurrent on the light intensity, and g) dependence of the responsivity on the light intensity of the $Cs_3Sb_2I_9$ MCs and film. h) High-resolution current versus time curve for the L-$Cs_3Sb_2I_9$ MCs.

of the $Cs_2AgBiBr_6$ film fabricated by spin coating as a control sample are also presented in Figures S8 and S9, Supporting Information, which suggests a phase-pure and compact film. The XRD results for the L-$Cs_3Sb_2I_9$ MCs fabricated using the PASE method are shown in Figure 4f. All the peaks originate from L-$Cs_3Sb_2I_9$ without any D-$Cs_3Sb_2I_9$ peaks, which suggests that phase-pure L-$Cs_3Sb_2I_9$ was obtained. The absorption spectrum of L-$Cs_3Sb_2I_9$ MCs is demonstrated in Figure 4g, indicating the absorption edge located at around 595 nm, where the bandgap of 2.08 eV can then be determined. The inset of Figure 4g shows the SEM image of a typical L-$Cs_3Sb_2I_9$ MC. The regular hexagonal shape corresponds to the $P\bar{3}m1$ space group, where the edge length was ≈60 μm. The HRTEM image of $Cs_3Sb_2I_9$ MCs is shown in Figure 4h, illustrating the lattice spacing of 0.32 nm, which is associated with the (222) plane of L-$Cs_3Sb_2I_9$. PL mapping was also performed, as shown in the inset of Figure 4f with the corresponding optical image. The PL intensity of the entire MC was uniform, indicating its high crystallinity. The thickness of L-$Cs_3Sb_2I_9$ MCs is then measured by AFM and shown in Figure 4i, which is about 1 μm. The surface morphology was also studied using AFM (Figure 4j). The surface undulation was only 2–3 nm, suggesting the great flatness of the MCs, and the RMS roughness was as low as 0.788 nm. The $Cs_3Sb_2I_9$ film fabricated by spin coating as a control sample was characterized by XRD and SEM, and the results are presented in Figures S10 and S11, Supporting Information. Peaks attributed to L-$Cs_3Sb_2I_9$ and D-$Cs_3Sb_2I_9$ were detected in the $Cs_3Sb_2I_9$ film's XRD result, indicating the mixed-phase nature of the film. The absorption edge of the film is located at 582 nm. In addition, there are obvious gullies in the SEM image of the film, which are the result of the evaporation of SbI_3 when the film is annealed.[18] AFM was also used to characterize the films thicknesses, where they are measured to be 212 and 626 nm for the $Cs_2AgBiBr_6$ and $Cs_3Sb_2I_9$ films, respectively, as shown in Figures S12 and S13, Supporting Information.

Subsequently, $Cs_2AgBiBr_6$ and L-$Cs_3Sb_2I_9$ MCs were configured as photodetectors, and their photoelectric performances were studied and compared with the corresponding control film devices. The I–V curves of the $Cs_2AgBiBr_6$ MCs photodetector were first characterized and are shown in Figure S14, Supporting Information, where the device was illuminated by a 450-nm laser with different light intensities. The close to perfect linear relationship in the I–V curves suggests the ohmic-like contact properties of the device, which is highly preferred for the efficient collection of photogenerated carriers. The I–t curves of the MCs and film photodetectors under modulated laser illumination with an intensity of 680 mW cm^{-2} were recorded and are shown in **Figure 5**a. The photocurrent of the MCs is more than two orders of magnitude larger than that of the film, which can be attributed to their superior crystallinity. Moreover, the dark current of the MCs is much lower than that of the film due to their low concentrations of defects and grain boundaries. These defects and grain boundaries usually constitute the main reasons for high dark currents in devices. Both the large photocurrent and low dark current contributed to the high on/off current ratio of >10^4. Figure 5b shows a linear correspondence relationship between the photocurrents and intensities of the incident light for both the MCs and spin-coated film. Accordingly, the LDR of the MCs and film photodetectors can be calculated to be as large as 100 dB. Responsivities as a function of light intensity are presented in Figure 5c. The largest responsivity of $Cs_2AgBiBr_6$ MCs reaches 3062 mA W^{-1}, which is more than 180 times larger than that of the film. The D* and EQE of the photodetectors can also be acquired using the equations mentioned earlier, and the results are shown in Figure S15, Supporting Information. The largest EQE of $Cs_2AgBiBr_6$ MCs is determined as 845%, and the largest D* reaches 3.3×10^{12} Jones. The EQE and D* values of the MCs were more than 180 and 520 times larger than those of the film, respectively. The response speed was also characterized based on the high-resolution I–t curve measured for $Cs_2AgBiBr_6$ MCs photodetectors (Figure 5d).

Table 1. Comparison of various figure of merits of AIHP-based photodetectors.

Halides	Method/Morphology	R [mA W^{-1}]	D^* [Jones]	Rise/decay time [ms]	References
CsPbI$_3$	Vapor/Nanowire	6.7	1.57×10^8	292/234	[31]
CsPbBr$_3$	Co-evaporation/Microwires	7660	4.05×10^{12}	275/550	[32]
CsPbBr$_3$	CVD/Microplatelets	1330	8.6×10^{11}	20.9/24.6	[33]
P3HT/PDPP3T/ CsPbBr$_3$/SnO$_2$	Solution/Nanowire array	250	1.2×10^{13}	0.111/0.306	[34]
spiro-OMeTAD/ CsPbBr$_3$/TiO$_2$	Solution/Quantum dots	10 100	9.35×10^{13}	2300/–	[41]
CsPbBr$_3$/PbSe	Solution/Quantum dots	6260	7.794×10^{12}	0.5/078	[42]
Cs$_3$Bi$_2$I$_9$	Solution/Single crystal	7.2	10^{11}	0.247/0.23	[43]
Cs$_3$Sb$_2$I$_9$	CVD/Microplates	40	1.26×10^{11}	0.096/0.058	[15]
Cs$_3$Bi$_2$Br$_9$/TiO$_2$	Solution/Film	6	3.39×10^{11}	0.57/0.58	[12]
Cs$_2$AgBiBr$_6$	Solution/Film	7010	5.66×10^{11}	0.956/0.995	[44]
Fluorine-doped tin oxide (FTO)/Bi-TiO$_2$/Cs$_2$AgBiBr$_6$/Ag	Solution/Film	11	10^{12}	0.0068/0.0055	[45]
Au/NiO/Cs$_2$AgBiBr$_6$/GaN/In	Solution/Film	33	10^{11}	0.151/0.215	[46]
CsPbBr$_3$	Solution/MCs	590 000	7×10^{13}	0.249/0.155	This work
Cs$_3$Sb$_2$I$_9$	Solution/MCs	670	1.7×10^{12}	0.149/0.158	
Cs$_2$AgBiBr$_6$	Solution/MCs	3062	3.3×10^{12}	0.188/0.182	

The rise and decay times of the device were determined to be 454 and 470 µs, respectively. Then, L-Cs$_3$Sb$_2$I$_9$ MCs and film photodetectors were studied and compared. The I–V curves of the MCs exhibit a linear relationship, again suggesting an ohmic-like contact (Figure S16, Supporting Information). The on–off switching characteristics of the L-Cs$_3$Sb$_2$I$_9$ MCs and film photodetectors with a light intensity of 730 mW cm^{-2} are depicted in Figure 5e. Obviously, the photocurrent of the MCs is much larger than that of the film, while its dark current is even lower than that of the film. As mentioned above, these observations can be ascribed to the superior crystallinity and lack of grain boundaries, and defects in MCs. The on/off current ratio of the L-Cs$_3$Sb$_2$I$_9$ MCs was greater than 10^4. Figure 5f shows the relationship between the MCs and film photocurrents and the intensities of the incident light. When the light intensity was lower than 10 mW cm^{-2}, the photocurrent of the L-Cs$_3$Sb$_2$I$_9$ MCs device exhibited a linear relationship. However, as the light intensity increased beyond 10 mW cm^{-2}, the photocurrent tended to saturate. This is because, for layered-material-based photodetectors, the LDR is not very large.[39,40] The LDR of L-Cs$_3$Sb$_2$I$_9$ MCs is then determined to be ≈60 dB. The LDR of the Cs$_3$Sb$_2$I$_9$ film photodetector was calculated to be as high as 100 dB. The responsivities under illumination with different light intensities are shown in Figure 5g. The largest responsivity of Cs$_3$Sb$_2$I$_9$ MCs reaches 670 mA W^{-1}, which is much larger than that of the film (80 mA W^{-1}). The D^* and EQE values of the photodetectors were also calculated and are shown in Figure S17, Supporting Information. The largest EQE of Cs$_3$Sb$_2$I$_9$ MCs is 185%, and the largest D^* reaches 1.7×10^{12} Jones, both of which are clearly larger compared to those of the film. Figure 5h shows the high-resolution I–t curve of the Cs$_3$Sb$_2$I$_9$ MCs photodetector. A response speed as fast as 188 µs was acquired. The performances of all AIHP-based photodetectors characterized in this work were compared with those reported recently, and the comparison is summarized in

Table 1. These results clearly demonstrate the technological potential of the solution-processing PASE method developed for the synthesis of high-quality AIHP materials for next-generation optoelectronic devices.

3. Conclusion

In summary, a facile low-temperature solution-processing PASE method was demonstrated and proven to be suitable for the synthesis of different types of AIHPs. The high-quality cubic CsPbBr$_3$, Cs$_2$AgBiBr$_6$, and L-Cs$_3$Sb$_2$I$_9$ MCs synthesized using this method can significantly enhance the performance of photoelectric devices. Importantly, all three AIHPs-based photodetectors were investigated in detail, and careful comparisons with their spin-coated film counterparts were conducted. Remarkably, all the AIHP MCs photodetectors show much superior performance to those of the film devices. For CsPbBr$_3$ MCs devices, the responsivity reaches values as high as 590 000 mA W^{-1}, and the detectivity is as high as 7×10^{13} Jones, which is far better than those of most previously reported single-crystal AIHP nanostructures. The Cs$_2$AgBiBr$_6$ and L-Cs$_3$Sb$_2$I$_9$ MCs photodetectors also exhibited impressive responsivities and detectivities. In addition, the response speed of these photodetectors can reach hundreds of microseconds, which is excellent for the AIHPs-based photodetectors. All these results suggest that the PASE method is a promising route to fabricate high-quality AIHPs, which can not only contribute to their further study but also drive their applications forward.

4. Experimental Section

Perovskite Precursor and PDMS Films Synthesis: 0.48 mmol CsBr and PbBr$_2$ were dissolved in 1 mL DMSO to prepare CsPbBr$_3$ solution;

1 mmol CsBr, 0.5 mmol AgBr, and 0.5 mmol $BiBr_3$ were dissolved in 1 mL DMSO to prepare $CsPbBr_3$ solution; 1 mmol CsI and 0.67 mmol SbI_3 were dissolved in 1 mL of DMF to prepare $Cs_3Sb_2I_9$ solution. The solutions were stirred at room temperature for 3 h to fully dissolve the chemicals, which were then filtered by a 0.2 μm polyvinylidene difluoride membrane before use. For the synthesis of PDMS films, silicone elastomer (PDMS) and its curing agent were mixed and blended uniformly at a weight ratio of 10:1, followed by the removal of air bubbles in a vacuum chamber. Afterward, the mixture with a thickness of 0.2 mm was spread in a petri dish and heated in an 80 °C oven for 4 h to get the PDMS film.

Device Fabrication: Glass or Si substrates were first ultrasonically cleaned with acetone, ethanol, and deionized (DI) water for 15 min. Oxygen plasma was then applied to these substrates to improve their hydrophilicity. For the PASE method, 3 μL of $CsPbBr_3$, $Cs_2AgBiBr_6$, or $Cs_3Sb_2I_9$ solution was dripped onto a hydrophilic substrate. After the solution was spread on the substrate for several seconds, it was covered with a PDMS film. The samples were then heated on a hot plate at 85 °C for 3 h. For the films fabricated by the spin-coating method, 30 μL of $CsPbBr_3$, $Cs_2AgBiBr_6$, or $Cs_3Sb_2I_9$ solution was spin-coated on a hydrophilic substrate at 3000 rpm for 40 s, followed by thermal annealing at 250 °C (for $CsPbBr_3$ and $Cs_2AgBiBr_6$) or 100 °C ($Cs_3Sb_2I_9$) for 10 min. For the spin-coating of $CsPbBr_3$, 100 μm of chlorobenzene was used as the antisolvent and dripped onto the substrate 15 s after the beginning of the spin-coating process to improve the crystallinity of the film. For the configuration of the photodetectors, shadow masks were used to thermally evaporate 50 nm thick Au electrodes with channel lengths and widths of 10 and 70 μm, respectively.

Samples and Device Characterization: XRD (D2 Phaser with Cu Kα radiation, Bruker) was used to characterize the crystal structure and phase of the obtained MCs and films. The morphologies of the MCs and films were studied by SEM (FEI Quanta 450 FEG SEM). The thickness and surface roughness of the MCs were investigated using AFM (Dimension Icon, Bruker, Santa Barbara, USA). The UV–vis absorption spectra of the MCs and films were measured using a Hitachi UH4150 UV–vis NIR spectrophotometer. The lattice structures of the MCs were investigated by HRTEM (FEI TECNAI G2 F30). PL and PL mapping were recorded using a Hitachi F-4600 spectrophotometer and a WITec RAMAN alpha 300R system, respectively. The photoelectrical performance of the photodetectors was characterized using a standard electrical probe station and an Agilent 4155C semiconductor analyzer (Agilent Technologies, California, USA) with a 450 nm laser used as the light source, while the power of the incident light was determined using a power meter (PM400, Thorlabs). The bias voltages in this work were fixed at 1.5 V for all *I–t* measurements of the photodetectors. To acquire the response times of the photodetectors, high-resolution *I–t* curves were measured using a low-noise current amplifier (SR570, Stanford Research Systems, USA) combined with a digital oscillator (TBS 1102 B EDU, Tektronix, USA).

Supporting Information

Supporting Information is available from the Wiley Online Library or from the author.

Conflict of Interest

The authors declare no conflict of interest.

Data Availability Statement

The data that support the findings of this study are available from the corresponding author upon reasonable request.

[1] H. Li, C. Chen, H. Hu, Y. Li, Z. Shen, F. Li, Y. Liu, R. Liu, J. Chen, C. Dong, S. Mabrouk, R. S. Bobba, A. Baniya, M. Wang, Q. Qiao, *InfoMat* **2022**, *1*, e12322.

[2] A. Fakharuddin, M. K. Gangishetty, M. Abdi-Jalebi, S. H. Chin, A. R. bin Mohd Yusoff, D. N. Congreve, W. Tress, F. Deschler, M. Vasilopoulou, H. J. Bolink, *Nat. Electron.* **2022**, *5*, 203.

[3] L. Mei, R. Huang, C. Shen, J. Hu, P. Wang, Z. Xu, Z. Huang, L. Zhu, *Adv. Opt. Mater.* **2022**, *10*, 2102656.

[4] J. Ghosh, P. J. Sellin, P. K. Giri, *Nanotechnology* **2022**, *33*, 312001.

[5] Y. Zhou, F. Lu, T. Fang, D. Gu, X. Feng, T. Song, W. Liu, *J. Alloys Compd.* **2022**, *911*, 165062.

[6] X. Sheng, Y. Li, M. Xia, E. Shi, *J. Mater. Chem. A* **2022**, https://doi.org/10.1039/d2ta02219b.

[7] T. Zhang, M. I. Dar, G. Li, F. Xu, N. Guo, M. Grätzel, Y. Zhao, *Sci. Adv.* **2017**, *3*, e170070.

[8] P. Gui, H. Zhou, F. Yao, Z. Song, B. Li, G. Fang, *Small* **2019**, *15*, 1902618.

[9] W. Zhu, M. Deng, D. Chen, Z. Zhang, W. Chai, D. Chen, H. Xi, J. Zhang, C. Zhang, Y. Hao, *ACS Appl. Mater. Interfaces* **2020**, *12*, 32961.

[10] Y. Zhong, K. Liao, W. Du, J. Zhu, Q. Shang, F. Zhou, X. Wu, X. Sui, J. Shi, S. Yue, Q. Wang, Y. Zhang, Q. Zhang, X. Hu, X. Liu, *ACS Nano* **2020**, *14*, 15605.

[11] C. Zhang, K. Wang, Y. Wang, W. S. Subhani, X. Jiang, S. Wang, H. Bao, L. Liu, L. Wan, S. Liu, *Sol. RRL* **2020**, *4*, 2000254.

[12] Z. Ji, Y. Liu, W. Li, C. Zhao, W. Mai, *Sci. Bull.* **2020**, *65*, 1371.

[13] Z. Zheng, Q. Hu, H. Zhou, P. Luo, A. Nie, H. Zhu, L. Gan, F. Zhuge, Y. Ma, H. Song, T. Zhai, *Nanoscale Horiz.* **2019**, *4*, 1372.

[14] B. Saparov, F. Hong, J. P. Sun, H. S. Duan, W. Meng, S. Cameron, I. G. Hill, Y. Yan, D. B. Mitzi, *Chem. Mater.* **2015**, *27*, 5622.

[15] S. K. Shil, F. Wang, Z. Lai, Y. Meng, Y. Wang, D. Zhao, M. K. Hossain, K. O. Egbo, Y. Wang, K. M. Yu, J. C. Ho, *Nano Res.* **2021**, *14*, 4116.

[16] B. Yang, Y. J. Li, Y. X. Tang, X. Mao, C. Luo, M. S. Wang, W. Q. Deng, K. L. Han, *J. Phys. Chem. Lett.* **2018**, *9*, 3087.

[17] J. Hebig, I. Ku, J. Flohre, T. Kirchartz, *ACS Energy Lett.* **2016**, *1*, 309.

[18] B. Saparov, F. Hong, J. Sun, H. Duan, W. Meng, S. Cameron, I. G. Hill, Y. Yan, D. B. Mitzi, *Chem. Mater.* **2015**, *27*, 5622.

[19] A. Singh, K. M. Boopathi, A. Mohapatra, Y. F. Chen, G. Li, C. W. Chu, *ACS Appl. Mater. Interfaces* **2018**, *10*, 2566.

[20] K. S. Chang, Y. C. Chung, T. H. Yang, S. J. Lue, K. L. Tung, Y. F. Lin, *J. Membr. Sci.* **2012**, *119*, 417.

[21] C. R. Tanardi, A. Nijmeijer, L. Winnubst, *Sep. Purif. Technol.* **2016**, *169*, 223.

[22] X. Zhang, Z. Tong, C. Liu, L. Ye, Y. Zhou, Q. Meng, G. Zhang, *ACS Omega* **2022**, *7*, 15786.

[23] C. Li, Z. Zang, C. Han, Z. Hu, X. Tang, J. Du, Y. Leng, K. Sun, *Nano Energy* **2017**, *40*, 195.

**ADVANCED
SCIENCE NEWS**

www.advancedsciencenews.com

**ADVANCED
OPTICAL
MATERIALS**

www.advopticalmat.de

[24] J. Zeng, X. Li, Y. Wu, D. Yang, Z. Sun, Z. Song, H. Wang, H. Zeng, *Adv. Funct. Mater.* **2018**, *28*, 1804394.

[25] C. Lan, R. Dong, Z. Zhou, L. Shu, D. Li, S. P. Yip, J. C. Ho, *Adv. Mater.* **2017**, *29*, 1702759.

[26] C. Lan, Z. Zhou, Z. Zhou, C. Li, L. Shu, L. Shen, D. Li, R. Dong, S. P. Yip, J. C. Ho, *Nano Res.* **2018**, *11*, 3371.

[27] R. Dong, C. Lan, X. Xu, X. Liang, X. Hu, D. Li, Z. Zhou, L. Shu, S. Yip, C. Li, S. W. Tsang, J. C. Ho, *ACS Appl. Mater. Interfaces* **2018**, *10*, 19019.

[28] Y. Zhang, Y. Liu, Z. Xu, Z. Yang, S. Liu, *Small* **2020**, *16*, 202003145.

[29] Y. Liu, H. Ye, Y. Zhang, K. Zhao, Z. Yang, Y. Yuan, H. Wu, G. Zhao, Z. Yang, J. Tang, Z. Xu, S. (Frank) Liu, *Matter* **2019**, *1*, 465.

[30] D. Yang, D. Ma, *Adv. Opt. Mater.* **2019**, *7*, 1800522.

[31] A. Waleed, M. M. Tavakoli, L. Gu, S. Hussain, D. Zhang, S. Poddar, Z. Wang, R. Zhang, Z. Fan, *Nano Lett.* **2017**, *17*, 4951.

[32] G. Tong, M. Jiang, D. Son, L. K. Ono, Y. Qi, *Adv. Funct. Mater.* **2020**, *30*, 2002526.

[33] Y. Li, Z. Shi, L. Lei, F. Zhang, Z. Ma, D. Wu, T. Xu, Y. Tian, Y. Zhang, G. Du, C. Shan, X. Li, *Chem. Mater.* **2018**, *30*, 6744.

[34] F. Cao, W. Tian, K. Deng, M. Wang, L. Li, *Adv. Funct. Mater.* **2019**, *29*, 1906756.

[35] Y. Meng, C. Lan, F. Li, S. Yip, R. Wei, X. Kang, X. Bu, R. Dong, H. Zhang, J. C. Ho, *ACS Nano* **2019**, *13*, 6060.

[36] H. Wang, D. H. Kim, *Chem. Soc. Rev.* **2017**, *46*, 5204.

[37] X. Yang, Y. Chen, P. Liu, H. Xiang, W. Wang, R. Ran, W. Zhou, Z. Shao, *Adv. Funct. Mater.* **2020**, *30*, 2001557.

[38] Z. Xiao, W. Meng, J. Wang, Y. Yan, *ChemSusChem* **2016**, *9*, 2628.

[39] Q. Liang, Q. Wang, Q. Zhang, J. Wei, S. X. Lim, R. Zhu, J. Hu, W. Wei, C. Lee, C. H. Sow, W. Zhang, A. T. S. Wee, *Adv. Mater.* **2019**, *31*, 1807609.

[40] Y. Tu, Y. Xu, J. Li, Q. Hao, X. Liu, D. Qi, C. Bao, T. He, F. Gao, W. Zhang, *Small* **2020**, *16*, 2005626.

[41] K. Shen, H. Xu, X. Li, J. Guo, S. Sathasivam, M. Wang, A. Ren, K. L. Choy, I. P. Parkin, Z. Guo, J. Wu, *Adv. Mater.* **2020**, *32*, ss202000004.

[42] J. Hu, S. Yang, Z. Zhang, H. Li, C. Perumal Veeramalai, M. Sulaman, M. I. Saleem, Y. Tang, Y. Jiang, L. Tang, B. Zou, *J. Mater. Sci. Technol.* **2021**, *68*, 216.

[43] Z. X. Zhang, C. Li, Y. Lu, X. W. Tong, F. X. Liang, X. Y. Zhao, D. Wu, C. Xie, L. B. Luo, *J. Phys. Chem. Lett.* **2019**, *10*, 5343.

[44] L. Z. Lei, Z. F. Shi, Y. Li, Z. Z. Ma, F. Zhang, T. T. Xu, Y. T. Tian, D. Wu, X. J. Li, G. T. Du, *J. Mater. Chem. C* **2018**, *6*, 7982.

[45] Y. Yuan, Z. Ji, G. Yan, Z. Li, J. Li, M. Kuang, B. Jiang, L. Zeng, L. Pan, W. Mai, *J. Mater. Sci. Technol.* **2021**, *75*, 39.

[46] S. Yin, Y. Cheng, Y. Li, W. Liang, T. Li, J. Ma, D. Wu, Z. Shi, X. Li, *J. Mater. Sci.* **2021**, *56*, 13633.